Si1-xGex alloys as negative electrode for Li-ion batteries: Impact of morphology in the Li + diffusion, performance and mechanism

A. Avila Cardenas, N. Herlin-Boime, C. Haon, L. Monconduit

▶ **To cite this version:**

A. Avila Cardenas, N. Herlin-Boime, C. Haon, L. Monconduit. Si1-xGex alloys as negative electrode for Li-ion batteries: Impact of morphology in the Li + diffusion, performance and mechanism. Electrochimica Acta, 2024, 475, pp.143691. 10.1016/j.electacta.2023.143691 . hal-04555148

HAL Id: hal-04555148
https://hal.science/hal-04555148

Submitted on 22 Apr 2024

HAL is a multi-disciplinary open access archive for the deposit and dissemination of scientific research documents, whether they are published or not. The documents may come from teaching and research institutions in France or abroad, or from public or private research centers.

L'archive ouverte pluridisciplinaire **HAL**, est destinée au dépôt et à la diffusion de documents scientifiques de niveau recherche, publiés ou non, émanant des établissements d'enseignement et de recherche français ou étrangers, des laboratoires publics ou privés.

$Si_{1-x}Ge_x$ alloys as negative electrode for Li-ion batteries: Impact of morphology in the Li^+ diffusion, performance and mechanism

A. AVILA CARDENAS,[1,2,5] N. HERLIN-BOIME,[3] C. HAON ,[2] L. MONCONDUIT[1,4,5,*]

[1] ICGM, University of Montpellier, CNRS, ENSCM, Montpellier, France

[2] Univ. Grenoble Alpes, CEA, Liten, LITEN, DEHT, 38000 Grenoble, France

[3] NIMBE, CEA-CNRS, UMR 3685, CEA Paris-Saclay, 91191 Gif sur Yvette

[4] Réseau sur le Stockage Electrochimique de l'Energie (RS2E), CNRS FR3459, Amiens, France

[5] ALISTORE-European Research Institute, Hub de l'Energie, FR CNRS 3104, 15 rue Baudelocque, 80039, Amiens, France

Abstract

$Si_{1-x}Ge_x$ alloys present interesting cycling performance as Li-ion anodes, owing to the synergetic effect from silicon's high capacity and germanium's electrical conductivity and Li^+ diffusion. Various morphologies of $Si_{1-x}Ge_x$ powders were obtained, micron-sized by ball-Milling (BM) and nano-sized by laser pyrolysis (LP) to study the effect of the morphology and composition on the electrochemical behavior. The electrical conductivity was measured and shows an increase with the Ge content, from 4.58E-03 for Si to 0.11 $S\ m^{-1}$ for $Si_{0.5}Ge_{0.5}$. Half-cells were cycled at C/5, LP samples showed a better capacity retention than their BM counterparts (88% vs 72% at the 35^{th} cycle for $Si_{0.5}Ge_{0.5}$). To rationalize these trends, Galvanostatic Intermittent Titration Technique (GITT) and Electrochemical Impedance Spectroscopy (EIS) were used to determine the apparent Li^+ Diffusion in the $Si_{1-x}Ge_x$ series. It was shown that the apparent Li^+ Diffusion is dependent to the state of charge. Moreover, it gave insight about phase transformations during cycling. During lithiation, similar values ($10^{-11}\ cm^2\ s^{-1}$) were obtained for BM and LP $Si_{0.5}Ge_{0.5}$. However, a big variation (10^{-13} – $10^{-10}\ cm^2\ s^{-1}$) was found for the BM sample delithiation, which is attributed to the delithiation of c-$Li_{15}(Si_{0.5}Ge_{0.5})_4$ phase into amorphous $Li_x(Si_{0.5}Ge_{0.5})$ ($x<3.75$). Asymmetric C-rate tests evidenced lithiation as the limiting mechanism for the $Si_{1-x}Ge_x$ negative electrodes.

1. INTRODUCTION

Since the establishment of the $LiCoO_2$/graphite electrochemical cell by Sony in 1991 as the reference Li-ion battery [1] (LIB), huge efforts have been made in both the material chemistry and cell engineering to fulfill the energy demands. The rise of electric vehicles (EVs) became a major driving force to develop new systems, which can increase the energy and power density and reduce the charging time while keeping a good cycle life and cost [2].

At the anode side, silicon has demonstrated to be a promising candidate owing to its high abundance and superior specific capacity (3579 mAh g^{-1} for $Li_{15}Si_4$ at RT) [3], almost ten times higher than graphite (372 mAh g^{-1} for LiC_6) [4] used in commercial LIBs. However, its implementation has been hindered because of its poor capacity retention. (De) lithiation of silicon results in a substantial volumetric expansion of approximately 300% [5], causing particle pulverization, delamination from the current collector and an unstable growth of the solid electrolyte interphase (SEI) with each cycle.

Although very expensive, germanium has attracted attention in the energy storage field due to its interesting specific capacity (1384 mAh g^{-1} for $Li_{15}Ge_4$ at RT), but mostly because it possesses a higher intrinsic electronic conductivity and lithium diffusivity compared to silicon.[6,7] Nevertheless, it presents the same problem of volume expansion when alloying with Li, with the difference of this being isotropic, which could explain the better cycle life of Ge [8].

For intrinsic semiconductor materials such as Si and Ge, the electrical conductivity at room temperature (3E-04 and 2 S m^{-1}, respectively) [9] depends on the charge carrier mobility and concentration. The diffusion coefficient of free dilute Li in bulk Si has been measured at 3E-14 cm^2 s^{-1} at room temperature from ion-drift experiments with *p-n* junctions [10]. For Ge, this value is about two orders of magnitude higher, measured in the range of 150 – 600˚C [11]. So far, the better cycling performance of Ge in respect to Si has been attributed to these two properties in the literature.

The Si-Ge phase diagram presents the advantage of being a full solid solution. The synergetic effect of Si and Ge association and the de-(lithiation) mechanism of the $Si_{1-x}Ge_x$ alloys have already been demonstrated. Ge contributes to a better capacity retention of the system in expense of the overall capacity. Thus $Si_{0.5}Ge_{0.5}$ showed the best capacity/cyclability compromise in the $Si_{1-x}Ge_x$ series [7,12,13]. Different Si-Ge materials have been investigated, such is the case of 2D siligane. They present an Li intercalation mechanism rather than an alloying mechanism, which avoid detrimental volume expansion [14]. An interesting composite of Ge/Si@NC/rGO was also prepared, taking advantage of the N-doped carbon and rGO to enhance the electronic and lithium ionic conductivity

respectively while alleviating the volume expansion; with a high capacity retention of 1302 mAh g^{-1} after 500 cycles at 1 A g^{-1} [15].

Different synthesis methods led to samples with different properties and morphologies. High-energy ball-milling (BM) is one of the most used techniques to synthesize Si-based alloys [16] since it is capable of attaining out of equilibrium phases. The obtained powder is partially amorphized and presents low crystallite size [13]. However, the samples are prone to contamination coming from the ball and jars and it is not scalable to industry. Laser pyrolysis (LP) produces well crystallized nanoparticles, with a spherical shape and agglomerated in a chain-like manner [12]. It has the advantage of having low pollution, efficient nucleation and being a partially scalable technique.

In this work, we used BM and LP as synthesis methods to study the impact of the morphology of a series of $Si_{1-x}Ge_x$ samples. The materials were investigated means of X-ray diffraction (XRD), Raman spectroscopy, electron microscopy and electrochemical techniques such as Chronoamperometry, Galvanostatic Cycling, GITT and EIS. The aim is to understand the role of Ge in the $Si_{1-x}Ge_x$ alloys.

2. METHODOLOGY

2.1 Material Synthesis

Micron sized $Si_{1-x}Ge_x$ (x = 0.1, 0.25, 0.5) samples were mechanically synthesized using high energy ball-milling (BM) with a SPEX 8000M miller. Silicon (Sigma Aldrich, 325 mesh, 99% purity) and germanium powders (Alfa Aesar, 100 mesh, and 99.99% purity) were introduced stoichiometrically in a stainless-steel jar under an Ar atmosphere. The mass ratio of stainless-steel balls to powder was fixed to 12. All samples were ground in 10 cycles of 100 min with 10 min breaks. Pure Si and Ge powders were also ball-milled as reference materials.
Nanosized $Si_{1-x}Ge_x$ (x = 0.1, 0.25, 0.5) samples were synthesized by laser pyrolysis (LP). Silane (Praxair, 99.999% purity) and germane (Air Liquide Deutschland GmbH, 20 wt% in He) gases were diluted in He (Air Products, 99.99% purity) and different gas ratio were mixed to achieve the different compositions. A high-power CO_2 laser (PRC SLS 2800) was operated in continuous mode, the power (measured at the reactor without the precursor gases) was fixed at 1050 W. The gas flows were monitored with mass flowmeters (Brooks Smart) and the pressure inside the reactor was maintained at 740 Torr. The nanopowders were transferred by an Ar flow to the filters where they were retained and collected.

2.2 Material Characterization

Powder X-ray diffraction (XRD) measurements were carried out on a Panalytical Empyrean diffractometer (Cu-Kα_1/Kα2 radiation, theta-theta configuration) with a silicon sample holder covered with a Kapton foil. The measured 2θ range was 20º - 80º with a step size of 0.033º and a duration of 1h. The recorded diffractograms were processed with the FullProf software for profile matching.

Raman spectra were collected using a LabRam Aramis (HORIBA Jobin Yvon) with an Ar^+ laser at a wavelength of 473 nm. Scanning was performed from 200-600 cm^{-1} with a D1 filter to avoid sample degradation.

Scanning Electron Microscopy (SEM) images were acquired with a FEI Quanta 200F Scanning Electron Microscope equipped with an Energy Dispersive X-ray (EDX) tube operating at 10 kV to access the morphology and elemental distribution of the ball-milled samples. Scanning Transmission Electron Microscopy (STEM) images were acquired with a FEI Titan Themis equipped with a SuperX EDX detector system operating at 200 kV to analyze the laser pyrolysis samples

The Brunauer, Emmett and Teller (BET) method was used to measure the specific surface area of the different powders using the Flowsorb 2300 analyzer (Micrometric).

Electrical conductivity measurements were performed using a homemade cell, which consisted of a polyoxomethylene (POM) cylindrical die fastened with stainless steel pistons. A known amount of powder was poured into the die and a pellet was formed using a hydraulic press (250 MPa). Chronoamperometry (CA) was used to apply a fixed voltage and the current response was recorded at room temperature. The resistivity was calculated from the thickness of the pellets, measured with a Mitutoyo micrometer.

2.3 Electrochemical tests

All electrodes were prepared with a composition of 70 wt% active material, 9 wt% of carbon fibers VGCF-H (Showa Denko) and 9 wt% of carbon black C65 (Timcal) as electronic percolators and 12 wt% of carboxymethylcellulose (CMC) (M_w = 250 kg mol^{-1}, D_s = 0.7, Sigma-Aldrich) as binder. The active material and carbon powders were placed into an agate vial and ground for 15 min at 400 rpm using a planetary ball-mill (Pulverisette 7) with a mass ratio of balls to powder of 10. The binder was diluted in 550 µL of deionized water and all the components were introduced into a plastic vial for mixing in a centrifuge (Kakuhunter) until obtaining homogenous ink. The slurry was cast onto an etched Cu foil (13 µm) with a doctor blade of 100 µm. The films were dried at room temperature and entered into a vacuum oven (80º C, -0.9 bar) overnight. Disk electrodes of 12.7 mm diameter were punched (mass loading 1.5 – 2 mg cm^{-2}) and dried in a Buchi vacuum oven at 80º C for 24 h before putting them inside an Ar filled glovebox.

CR2032 coin cells were assembled inside an Ar filled glovebox. The different materials were tested in half-cells as working electrodes and Li metal (MTI) was used as counter electrode. The electrolyte was composed of 1M $LiPF_6$ (Solvionic) dissolved in ethylene carbonate and dimethyl carbonate (EC/DMC, 1:1 v/v) with 2 % vinyl carbonate (VC) and 10 % fluoro ethyl carbonate (FEC) as additives. A glass microfiber filter (Whatman GF/D) was used as a separator. All electrochemical tests were performed on a BCS-805 (Biologic) potentiostat at room temperature. All batteries were submitted to one formation cycle at C/20.

The current density for each of the different $Si_{1-x}Ge_x$ samples was set from their theoretical specific capacity; at 1C: 2 A g^{-1}, 2.56 A g^{-1} and 3.1 A g^{-1} for $Si_{0.5}Ge_{0.5}$, $Si_{0.75}Ge_{0.25}$ and $Si_{0.9}Ge_{0.1}$ respectively. Galvanostatic Cycling with Potential Limitation (GCPL) was carried out at C/5 in a range of 1.5 V – 10 mV *vs* Li^+/Li.

Galvanostatic Intermittent Titration Technique (GITT) and Electrochemical Impedance Spectroscopy (EIS) were performed in the same system. A low current (C/20) was applied for 30 min for each titration step accompanied by a 2 h rest period to reach equilibrium. The EIS spectra was recorded after each resting period in a frequency range of 10 kHz – 0.1 Hz under an AC-input with a 5 mV amplitude, followed by an open circuit voltage (OCV) period of 5 min. The second cycle was recorded following this procedure with a voltage range of 1.5 V – 50 mV. Zview software was used to treat and fit the data.

Asymmetric C-rate testing was performed by lithiating at a fixed C/10 rate and varying the delithiation rate from C/10 to 5C (5 cycles for each rate), and vice versa. The potential range was 1.5 V – 100 mV.

3. RESULTS AND DISCUSSION

3.1 Characterization of the $Si_{1-x}Ge_x$ alloys

The X-ray powder patterns of the $Si_{1-x}Ge_x$ samples synthesized by BM and LP are shown in Figure 1a. The alloys prepared by BM show broader Bragg peaks than the LP, due to a decrease of crystallite size (5.3 nm versus 14.5 nm for the $Si_{0.5}Ge_{0.5}$ composition) coming from the high energetic milling as confirmed by the crystallite size calculations from Scherrer's equation (TS1). The cell parameters of pure Si (*a = 5.429(5) Å*) and Ge (*a = 5.657(2) Å*) were refined by profile matching (FullProf suite) and agree with those reported

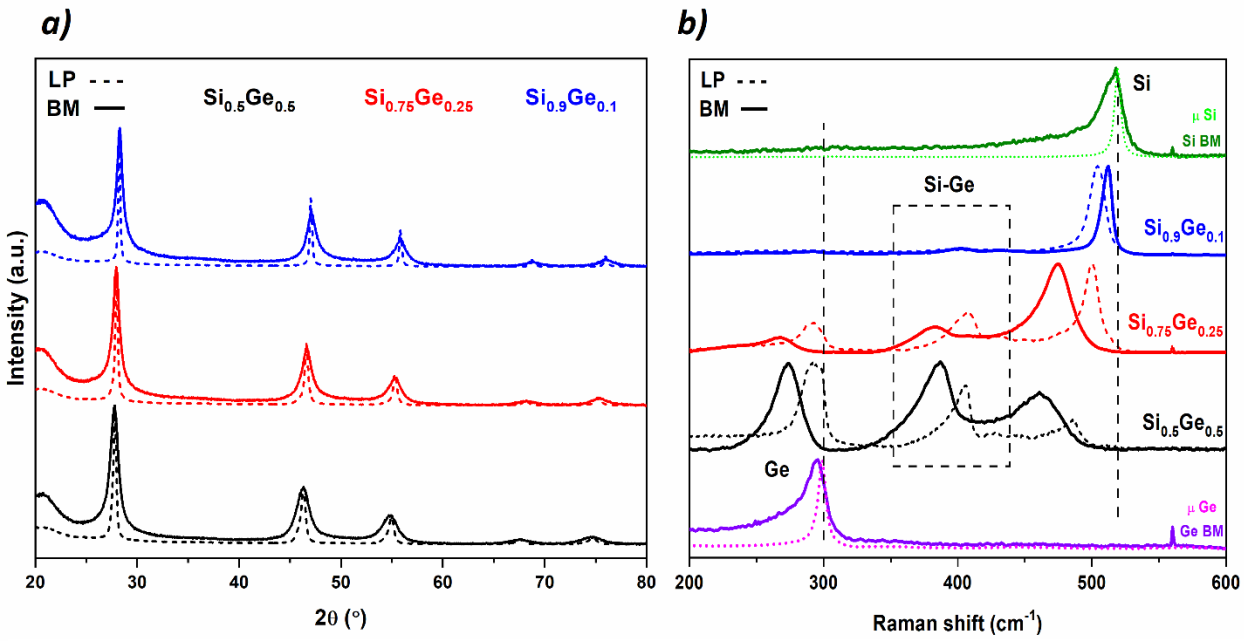

Figure 1. XRD (a) and Raman spectra (b) of BM and LP $Si_{1-x}Ge_x$ (x = 0.1, 0.25, 0.5) samples.

by the ICSD (00-027-1402 and 00-004-0545, respectively). The cell parameters of the intermediate alloys follow a linear increase with the addition of Ge, which is in agreement with Vegard's law and evidences the typical solid solution behavior in $Si_{1-x}Ge_x$ alloys (S1) [13].

The Raman spectra of the BM and LP samples are displayed in Figure 1b. For the pure Si and Ge powders, the signature bands of Si (519 cm^{-1}) and Ge (299 cm^{-1}) correspond to the homogeneous bond vibrations in the material. It is possible to obtain information on the local organization of the material from the peaks shape and position. For the ball-milled Si and Ge, the broadening of the active bands and the emergence of a shoulder in the lower frequency region suggest a partial amorphization of the sample during ball milling due to the lack of long-range order [17,18]. The intermediate samples show an evolution of the bands and the appearance of the Si-Ge band in the middle region (375 – 425 cm^{-1}). The shifting of the peaks to lower frequency values is related to the homogeneity of the material. For the $Si_{0.5}Ge_{0.5}$ and $Si_{0.75}Ge_{0.25}$ samples, the BM alloys show wider bands with lowered shifts compared to the LP, indicating a higher amorphous contribution and more heterogeneous composition. Surprisingly, for the $Si_{0.9}Ge_{0.1}$ stoichiometry, it is the LP sample showing these features. This could be attributed to heterogeneities during the synthesis and the existence of a composition gradient in the compound [12].

The morphology of the $Si_{0.5}Ge_{0.5}$ alloy is presented in Figure 2. The BM sample (left) consists on submicron and micrometer particles, which agglomerate into clusters of 5-10 µm. The EDX mapping shows a homogeneous distribution of the elements in the material and the Si/Ge ratio corresponds to the stoichiometric value. The LP (right) shows a very distinct structure, with sphere-like nanoparticles (89 ± 21 nm) which agglomerate into chains. It is possible to distinguish the Si-rich shell and SiGe core from the STEM-EDX images. We can observe pure Si nanoparticles (10-30 nm) as aggregates in the SEM images, which are formed by the partial decomposition and nucleation of silane molecules before thermalization of the reactive medium by collisions [12]. The Si/Ge ratio for the LP is close to the stoichiometric value, but the difference could come from a more heterogeneous material owing to the presence of different alloy phases in the sample.

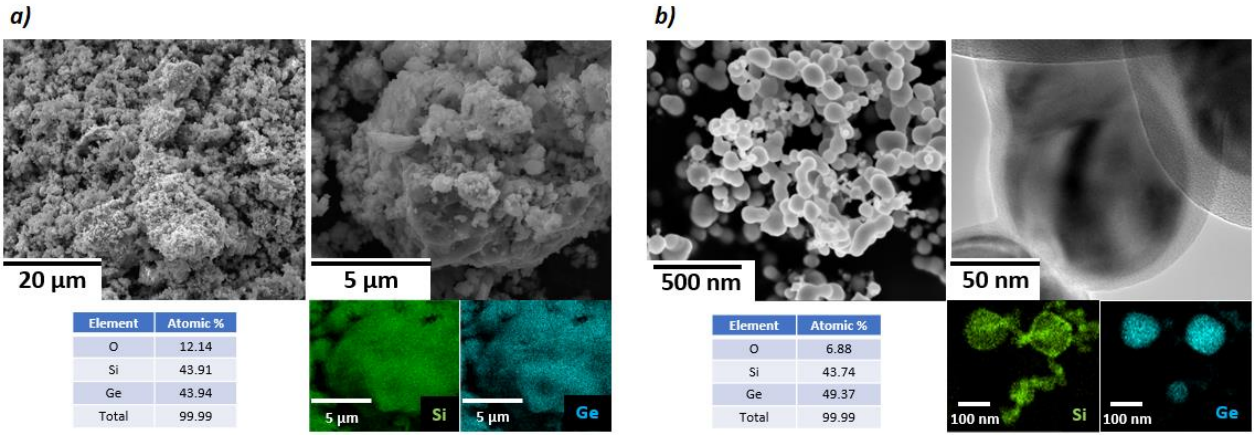

Figure 2. SEM images and EDX/STEM-EDX mapping of the BM (a) and LP (b) $Si_{0.5}Ge_{0.5}$ sample.

The electrical conductivity measurements for the $Si_{1-x}Ge_x$ pelletized powders are calculated using the formula [19]:

$$\sigma_{el} = \frac{l}{R \cdot S}$$

With l (m) and S (m^2) as the thickness and surface area of the pellet and R (Ω) being the resistance to the applied current through the pistons. The values are given in Table 1. For the micron-sized particles synthesized by BM, we can notice as expected a trend of increasing conductivity with the addition of Ge. It is worth noting that iron impurities from the stainless-steel jar, as identified by EDX (less than 1 at %), can partially contribute to this high conductivity values. Pure Si and Ge micron powders were measured as references, with electrical conductivities of 7.75E-05 and 0.61 $S\ m^{-1}$ respectively, proving that the obtained values for the BM samples are indeed influenced to some extent by the Fe impurities. In the case of the nano sized LP particles, the values are about five orders of magnitude lower than BM and show no clear relation to the amount of Ge. We suppose that in that case the conductivity of nanoparticles is influenced drastically by the inter-particle transport rather than by the bulk material feature [20]. Moreover, it has been demonstrated that the effective electrical conductivity for metal powders under compression depends on several parameters, such as the mean thickness of the native oxide layer, the particle radius and the presence of coating layer [21]. Thus, our conductivity measurement setup is not well adapted to know the real electrical conductivity of the SiGe@Si core-shell nanoparticles.

Table 1. Electrical conductivity of the $Si_{1-x}Ge_x$ samples measured by Chronoamperometry.

	Electrical conductivity (S m^{-1})				
$Si_{1-x}Ge_x$	*x = 0*	*x = 0.1*	*x = 0.25*	*x = 0.5*	*x = 1*
BM	4.58E-03	0.01	0.02	0.11	15.32

3.2 Electrochemical tests

The galvanostatic profiles of the BM and LP $Si_{1-x}Ge_x$ (x=0.1, 0.25, 0.5) electrodes along with their derivative curves are presented in Figure 3 and 4. A similar discharge/charge profile is observed for both type of materials, with a pseudo plateau in the first lithiation around 0.1-0.25 V (seen as broad peaks in the derivative curves), a plateau during delithiation at approximately 0.45 V (sharp peaks which signal the formation of c-$Li_{15}M_4$ phase in discharge) [7] and a sloping plateau in the second lithiation in the range of 0.1-0.4 V (indicating the amorphization of active material at the end of charge). The voltage hysteresis (distance between the main derivative peaks) decreases with the addition of Ge, passing from 0.31 up to 0.23 V in the $Si_{1-x}Ge_x$, which could be connected to higher electrical conductivity in Ge rich samples. In the first lithiation, LP materials show a flatter plateau than BM samples, which can be linked to the higher crystallinity of LP $Si_{1-x}Ge_x$, as it can be seen from the XRD and Raman characterizations. It has been reported that the electrochemical lithiation of amorphous Si undertakes a smoother physical transformation than its crystalline counterpart, with a single phase mechanism (sloping plateau from 0.4 to 0.1 V) rather than the biphasic transition (flat plateau around 0.1V) respectively [22–24]. Another relevant feature is found at the beginning of the delithiation curve of the LP electrodes, the sloppier plateau for the Si-rich material, x=0.9, agrees with the cycling

profiles for pure Si nanomaterials [25,26] and indicates less amount of the c-$Li_{15}M_4$ phase

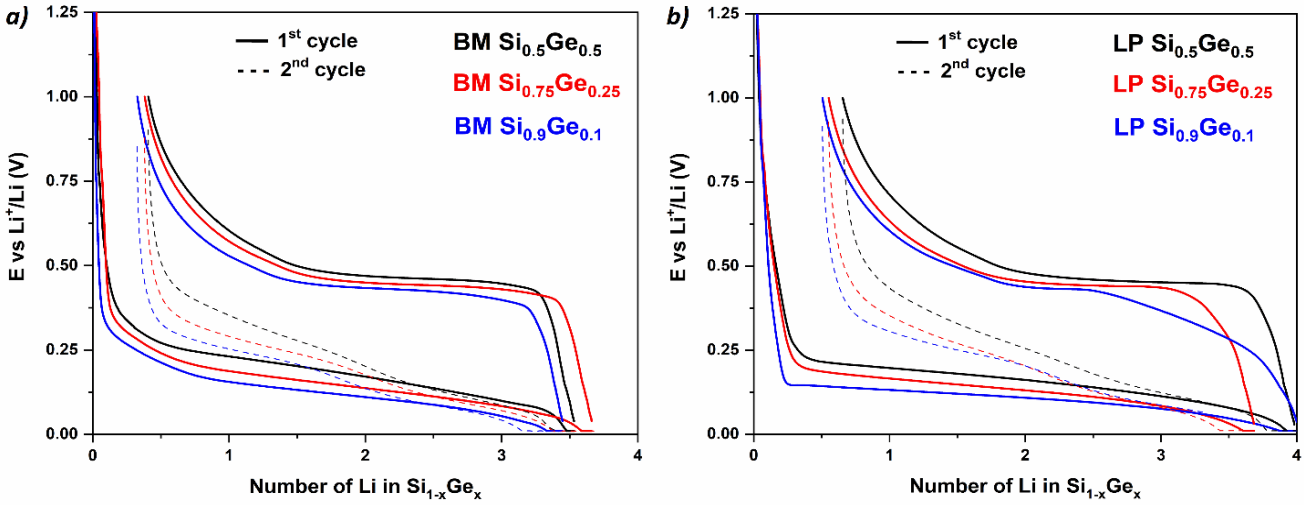

Figure 3. Galvanostatic curves of the BM (a) and LP (b) $Si_{1-x}Ge_x$ (x = 0.1, 0.25, 0.5) cycled at C/20 Vs Li.

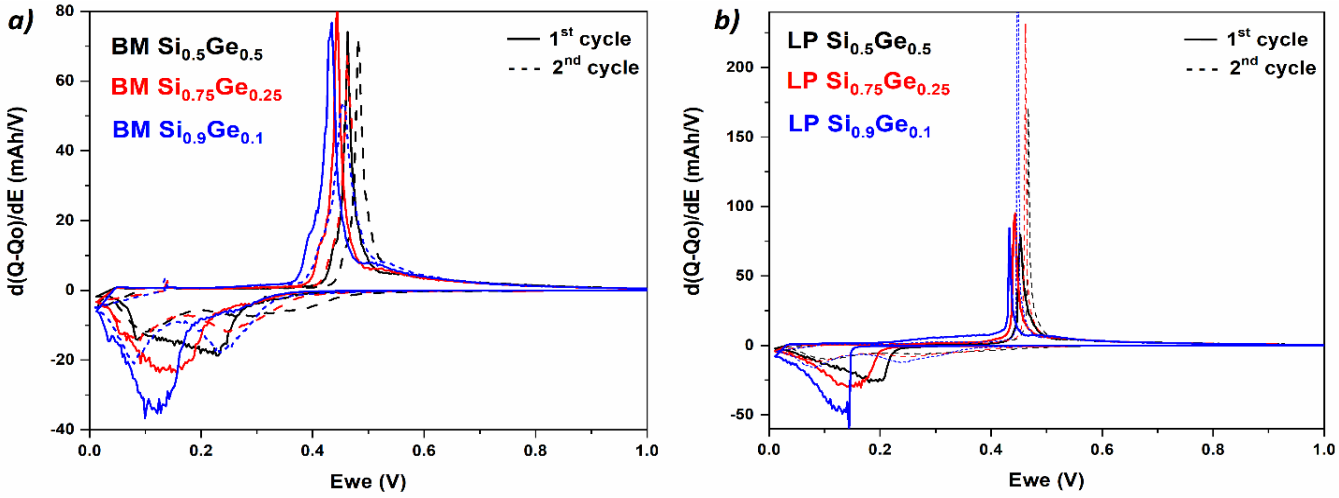

Figure 4. Derivative curves of the BM (a) and LP (b) $Si_{1-x}Ge_x$ (x = 0.1, 0.25, 0.5) first and second cycles.

was formed during the lithiation step.

A comparison between BM Si and Ge can be found in Figure S2. The voltage profiles (left) show the characteristic lithiation/delithiation mechanisms and the capacity retention tests (right) demonstrates the poor performance of Si.

The capacity retention tests for the different stoichiometries are presented in Figure 5 along with the Coulombic efficiency. The discharge capacity is normalized and plotted from the second cycle in order to compare both systems without considering the initial loss of capacity coming mainly from the SEI formation. Both type of materials show an improvement with the higher content of Ge, with a much better capacity retention for the

LP samples, owing to the particle size, which is below the critical diameter of 150 nm, avoiding the particle pulverization during cycling [27]. We observe a trend for the initial Coulombic efficiency (ICE), with an increase of the values for the less Ge containing alloys, pointing out the different electrochemical nature of the Si and Ge elements. In addition, ICE values are higher for the BM powders (88.5% against 83.6% respectively, for the $Si_{0.5}Ge_{0.5}$ composition) likely due to their smaller specific surface area compared to the LP analogues (as evidenced from the BET measurements (TS2)), which leads to less SEI formation. The CE is steady only for the BM $Si_{0.5}Ge_{0.5}$, while all LP samples (x=0.1, 0.25 and 0.5) show a better stability. It is worth noticing also that a significant drop in CE is observed for the Si-rich BM samples, which is likely linked to the severe capacity drop. The CE increases again when the capacity has lost approximately 40% of its starting value. Therefore, the lithiated alloys formed involve much less volume expansion, the formation of SEI is reduced (less fresh surface) and the CE rises. Moreover, the big particles are more prone to pulverization and particle disconnection.

The worse performance of the BM samples can be linked to the bigger size of the particles, since they are prone to shatter when they reach the fully lithiated state and form the c-$Li_{15}M_4$ phase. As consequence, new surface will be exposed to electrolyte and a continuous formation of solid electrolyte interphase (SEI) will take place, consuming high amount of Li in the system. Further problems come from the disconnection in between the different components of the electrode and from the current collector, decreasing the accessible active material and lowering the cell capacity. The reversible capacities measured for each material are summarized in Table 2, and compared to the theoretical values (calculated from the $Li_{15}M_4$ phase formation) for the different $Si_{1-x}Ge_x$ (x = 0.1, 0.25 and 0.5; 3089, 2562 and 1996 mAh g^{-1} respectively).

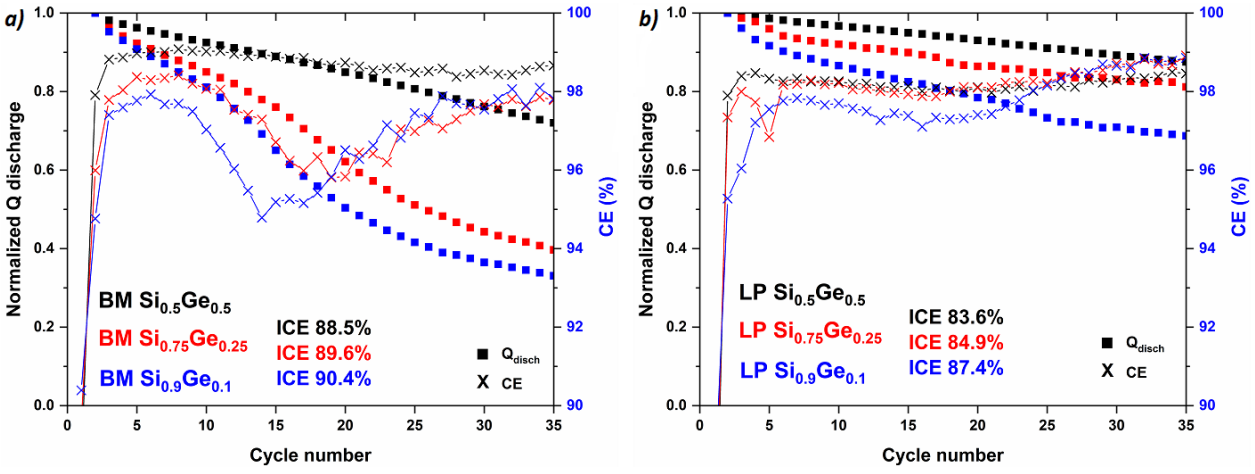

Figure 5. Discharge capacities normalized to the second cycle of the BM (a) and LP (b) $Si_{1-x}Ge_x$ (x = 0.1, 0.25, 0.5) cycled at C/5 Vs Li and their respective Coulombic efficiencies.

Table 2. ICE, theoretical and experimental discharge capacities of the first cycle BM and LP Si1-xGex (x = 0.1, 0.25, 0.5) samples, cycled at C/5 vs Li.

$Si_{1-x}Ge_x$	Theoretical Capacity (mAh g^{-1})	**BM**		**LP**	
		Capacity (mAh g^{-1})	*ICE*	Capacity (mAh g^{-1})	*ICE*
$Si_{0.9}Ge_{0.1}$	*3089*	*2495*	*90.4*	*2883*	*87.4*
$Si_{0.75}Ge_{0.25}$	*2562*	*2241*	*89.6*	*2123*	*84.9*
$Si_{0.5}Ge_{0.5}$	*1996*	*1664*	*88.5*	*1771*	*83.6*

To get deeper in the understanding of the electrochemical trends observed for BM and LP $Si_{1-x}Ge_x$ series, and investigate how each specific morphology affects the Li ion diffusivity, GITT and EIS were performed. The apparent Li^+ diffusion coefficient can be estimated at different states of charge according to the following equations [25,28]:

$$D_{Li+} = \frac{1}{2}\left[\left(\frac{V_M}{SFA}\right)\left(\frac{\delta E}{\delta x}\right)\right]^2 \qquad EIS$$

$$D_{Li+} = \frac{4}{\pi\tau}\left[\left(\frac{nV_M}{S}\right)\left(\frac{\Delta E_s}{\Delta E_t}\right)\right]^2 \qquad GITT$$

Where V_M $(cm^3 mol^{-1})$ is the molar volume of the compound, F $(96{,}485\ C\ mol^{-1})$ is the Faraday constant, n (mol) is the number of moles and S (cm^2) is the interfacial area between the electrode and the electrolyte, which will be taken as the geometrical for simplicity. In the EIS equation, A $(\Omega\ s^{-0.5})$ is the Warburg coefficient, calculated from the slope of the imaginary part of the impedance plotted against $1/\sqrt{2\pi f}$ and $\delta E/\delta x$ (V) is the slope of the galvanostatic curve. In the GITT equation, τ (s) is the titration time, ΔE_s (V) is the steady-state voltage change and ΔE_t (V) is the voltage change during the current pulse.

For lithium active alloys, such as in the case of Si and Ge, it is important to consider the change in the molar volume as function of the Li content, expressed as a linear relationship:

$$V_M(x) = V_o + kx$$

Where V_o is the unlithiated molar volume of the compound, k is the constant molar volume of Li in Si/Ge $(9\ cm^3 mol^{-1})$ and x is the number of moles of Li. In the case of Si, the linear expansion has been confirmed by atomic force microscopy at room temperature [29]. The voltage profile of the $Si_{0.5}Ge_{0.5}$ composition is displayed in Figure 6a. As stated in the experimental section, a formation cycle is applied to avoid the distorted diffusion coming from the transformation of a crystalline material into an amorphous one in the first cycle. During the second lithiation, we observe a sloping plateau, which reveals the amorphization

of both materials. However, it is possible to discriminate the behavior of the samples on the subsequent delithiation, with a tilted plateau for the LP material and a horizontal one for the BM. This confirms the higher susceptibility of micron sized particles to crystalline phase ($Li_{15}M_4$) formation under these electrochemical conditions.

The apparent Li^+ diffusion coefficients as function of the state of charge are presented in Figure 6b for both BM and LP $Si_{0.5}Ge_{0.5}$ stoichiometry. We observe a good correspondence between the values obtained from GITT and EIS, with some differences in the magnitude at the end of the lithiation which are suspected to come from the specific technic limitations. From the Nyquist plots (S4 and S5) it can be observed that the diffusion tail for the SOC between 0.75 – 1 tend to curve towards the real impedance axis, no longer maintaining the straight slope, because of an augmented electrical conductivity nature of the highly lithiated electrodes.
The D_{Li+} for Si measured at room temperature from GITT and EIS ranges from 10^{-13} - 10^{-10} cm^2 s^{-1} according to literature [5], which is comparable to our results. For Ge, the experimental results with similar techniques are of similar order of magnitudes, in the range of 10^{-12} - 10^{-10} cm^2 s^{-1} at ambient temperature [30,31].

From the shape of the apparent $D_{Li+,}$ we can conclude that there is not a linear relationship with the content of Li. Typically, a "W" pattern is ascribed in both senses of charge/discharge, where the minima correspond to the phase transitions of the compound as it alloys with Li [5,28]. The BM sample shows the expected pattern for lithiation, with a smooth conversion of the amorphous phase intermediates which we ascribe as *a-Li_xM* (with x close to 1) and *a-$Li_{13}M_4$* according to chemical species reported in the literature [7], and values around 10^{-11} cm^2 s^{-1}. During delithiation, the behavior is altered, with a drop of three order of magnitudes from 10^{-10} to 10^{-13} cm^2 s^{-1}, which we believe is caused by the rough transition of the *c-$Li_{15}M_4$* to the *a-Li_7M_3* phase. For the LP sample, the trend is more conventional, with a mild transformation of the phase intermediates and a reversible diffusion path for lithiation/delithiation, attaining coefficients of 10^{-11} cm^2 s^{-1}. These results put into evidence that the size/morphology of the material plays a critical role on the phase transformations of $Si_{1-x}Ge_x$ alloys during Li insertion and directly influences the Li^+ diffusion path.

An equivalent experiment was performed for the BM Si and Ge to understand how the nature of the material can influence the diffusion coefficient and the lithiation/delithiation mechanism. Figure S3 contains the voltage profile of the GITT experiment, where it is possible to witness the distinct behavior of the two elements. The micron sized Si (BM) presents the standard "W" shape and apparent D_{Li+} in the range of 10^{-12} – 10^{-9} cm^2 s^{-1}, with minima attributed to *a-LiSi* and *a-$Li_{13}Si_4$*. BM Ge depicts a different pattern, with a rough transition during delithiation (similar to the BM $Si_{0.5}Ge_{0.5}$ sample) and surprisingly, values one order of magnitude lower than its Si counterpart. The minima are associated with *a-Li_xGe* intermediates and *a-Li_9Ge_4* phases [7,32]. This experimental data indicates that Li ion diffusion is greatly limited by the phase transformations of the alloying compound, as Ge is more prone to form the c-$Li_{15}M_4$ phase under these electrochemical conditions than Si.

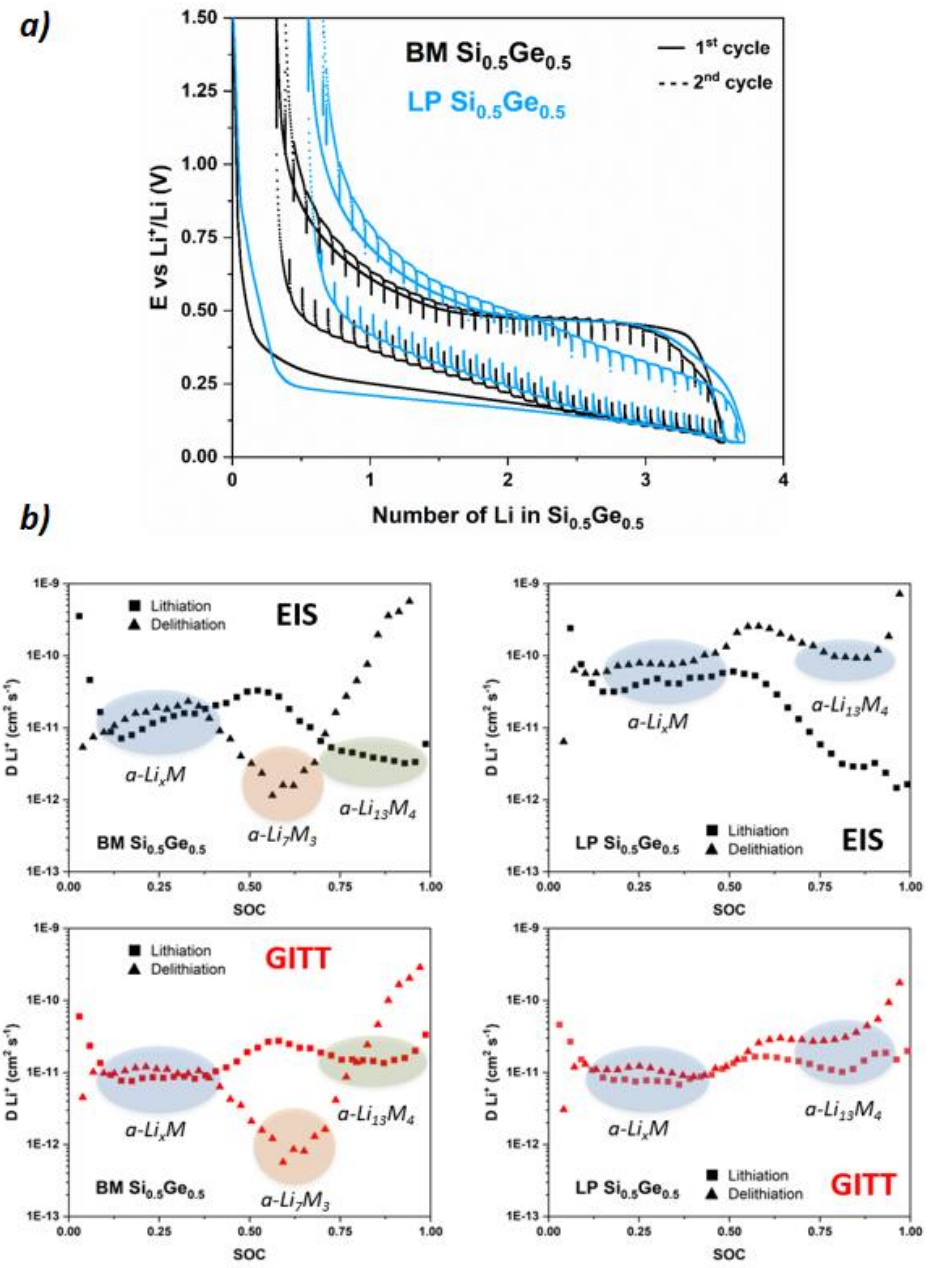

Figure 6. GITT profile of the BM and LP Si0.5Ge0.5 half-cells at C/20 Vs Li (a). Apparent Li+ diffusion (b) as function of the SOC measured by EIS (top) and GITT (bottom).

In general, the BM and LP $Si_{0.5}Ge_{0.5}$ behave in a similar way during lithiation, showing akin values of the apparent D_{Li+}. Yet, there is significant variation on the delithiation path for the BM sample, with different amorphous intermediates (a-Li_7M_3) being formed and apparent D_{Li+} up to two orders of magnitude lower than LP. This confirms the non-

reversible mechanism of the micron sized material under the same electrochemical conditions. In the same manner, it is the BM Ge which presents the largest contrast between lithiation and delithiation, and to our surprise, ten times lower D_{Li+} than those of BM Si. Additionally, it is the delithiation mechanism which presents globally higher D_{Li+} values, except when the rough transition from the c-$Li_{15}M_4$ phase to the amorphous intermediate occurs, and we further investigate its impact on the performance in the following section. It has been pointed out that the difference in diffusion could be attributed to the behavior of Si/Ge, which experiences compressive stress during lithiation and tensile strength during delithiation [33].

Asymmetric cycling tests were carried out in order to find out the limiting mechanism in the $Si_{1-x}Ge_x$ system. The cycling protocol consisted on fixing the lithiation (discharge) or delithiation (charge) rate at C/10 (200 mA g^{-1}) while simultaneously the delithiation or lithiation rate, respectively, were varied from C/10 to 5C (10 A g^{-1}). In Figure 7a, we can see the normalized discharge capacity retention of the BM and LP $Si_{0.5}Ge_{0.5}$ material submitted to these different current C-rates. It is obvious that the LP sample performs better than its BM equivalent, with 60% of the initial discharge capacity in the 50th cycle instead of 30%. In both samples, fixing the lithiation rate show the best results with a retained capacity of 60% and 25% at 5C, which proves the better performance of the nanosized material and for the latter a good tolerance to delithiate at high rate. Neither of the materials could deliver relevant capacity under fixed delithiation and a lithiation rate from 2C. As expected, the lithiation mechanism limits the high-rate capability of this system, since a moderate current is necessary to guarantee the complete lithiation of the compound and with it the full extent of the capacity in the subsequent cycles.

Figure 7b displays the derivative curves of the first, 2nd, 35th and 50th cycle in these conditions. We observe that with 100 mV potential cutoff, the sharp peak at 0.44 V for the BM sample in the first charge disappears and is replaced for two broad peaks around 0.3 V and 0.47 V in the second cycle. In the case of the LP material the sharp peak is not present at all, indicating that other mechanism occurs during lithiation/delithiation to form amorphous intermediate phases. This confirms the importance of the voltage cap to limit the c-$Li_{15}M_4$ phase formation in the system, since this phase has been pointed out to be linked to low CE and poor long cycling performance [26,34,35]. The derivative peak positions in the 35th cycle allow us to extract the voltage hysteresis of the cells at 5C (distance between the lithiation peak at 0.28V and the delithiation peaks at 0.88V for LP and 1.01V for BM), which is approximately 0.13 V lower for the LP than BM, in agreement with the better performance of the nanoparticles at high-rate. The hysteresis during charge/discharge, characteristic of both alloying and conversion materials, unlikely to insertion type materials, has been related to the energy barrier to break and form new chemical bonds in the system [33]. Note that the energy barrier to delithiate the crystallized $Li_{15}M_4$ phase in BM sample, to convert it in less lithiated amorphous material in charge, is expected to be higher than that needed to delithiate amorphous Li_xSi ($x<3.75$) in LP phase. As consequence the lithiation/delithiation is easier in the LP system, as evidenced from the smoother D_{Li+} pathway.

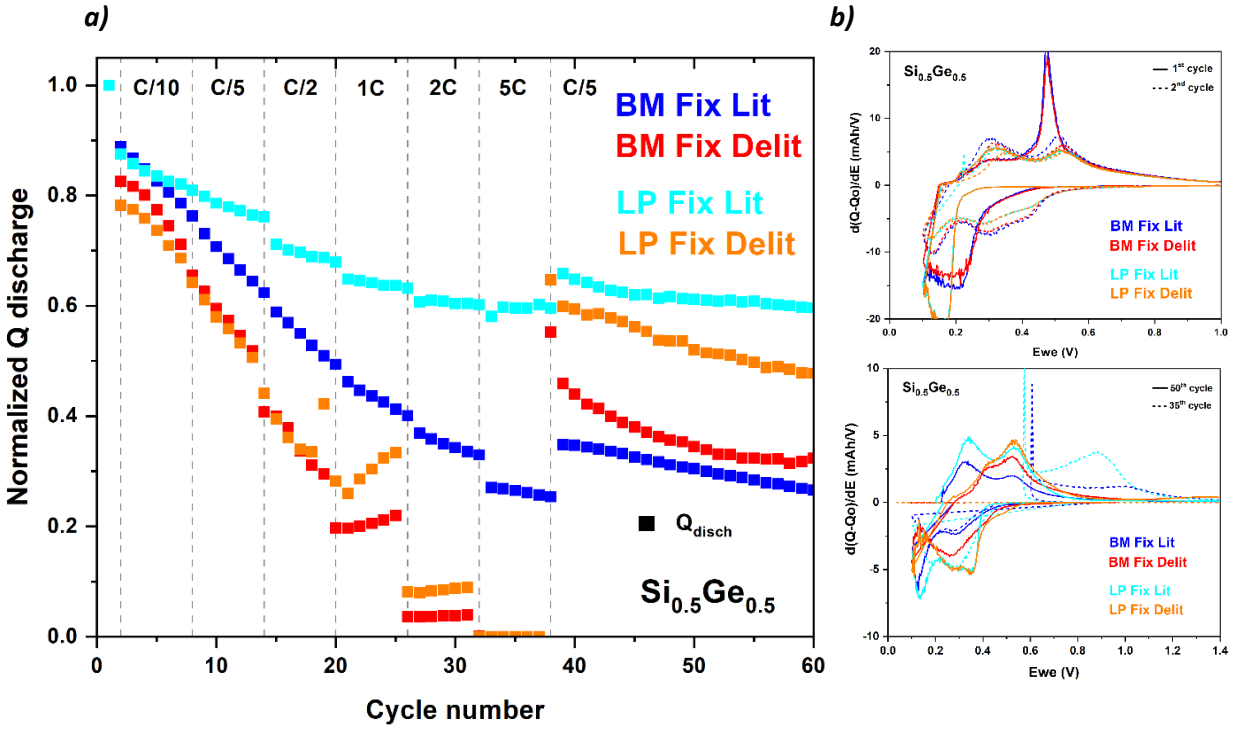

Figure 7. Asymmetric C-rate tests (a) of BM and LP $Si_{0.5}Ge_{0.5}$ half-cells Vs Li. Derivative curves (b) of the 1st, 2nd, 35th and 50th cycle.

4. CONCLUSION

An extensive investigation was carried out by comparing $Si_{1-x}Ge_x$ alloys samples synthesized by high-energetic ball-milling and laser pyrolysis. XRD and Raman showed similar features for both type of samples, with a higher amorphization degree for the milled powders. Through SEM/STM/EDX, the distinct morphology was put into evidence, with micron-sized clusters for BM and nano SiGe core/Si-rich shell for the LP materials.

Galvanostatic cycling demonstrated the better capacity retention for the LP counterpart, even if the ICE was smaller, a known feature for the nano sized particles with higher surface area.

Superior electrical conductivity was obtained for the Ge containing alloys, up to four order of magnitudes higher than pure Si, showing a trend of better electrochemical performance as the content of Ge increased. GITT coupled with EIS enabled the calculation of the apparent diffusion coefficient of Li through the electrodes, showing a strong dependence on the Li content. Both BM and LP showed values around 10^{-11} cm^2 s^{-1} during lithiation. However, during delithiation the micron-sized BM sample showed rough variation of the diffusion coefficient, likely due to the bigger sizes particles more prone to form the crystalline $Li_{15}M_4$ phase during discharge. The technique also allowed tracking the

formation of amorphous intermediates during de (lithiation), which agrees with some of the phases detected experimentally by other researchers [5,7,28,32].

Surprisingly for BM Si and Ge, the here calculated apparent D_{Li+} for Ge was one order of magnitude lower than that of Si, contrary to the expected results [36]. Ge proved to be more sensitive to the formation of the crystalline $Li_{15}M_4$ than Si, under the same experimental conditions.

Asymmetric C-rate tests provided information on the limiting mechanism during charge/discharge. On both BM and LP $Si_{1-x}Ge_x$ electrodes, lithiation is confirmed to be the restrictive process, with however better performance for the nanosized LP materials.

It seems that the apparent D_{Li+} is not the primary property to explain the better electrochemical behavior of LP and it might be pointed out that size and the formation of the crystalline/amorphous intermediates are the main responsible. The cycling protocol, specifically the voltage cutoff, plays an important role in the c-$Li_{15}M_4$ formation and determines to some extent the cyclability of the system.

Acknowledgment

As part of the DESTINY PhD programme acknowledges funding from the European Union's Horizon2020 research and innovation programme under the Marie Skłodowska-Curie Actions COFUND - Grant Agreement No: 945357. The authors would like to acknowledge CEA for the financial support. The authors gratefully acknowledge the French National Research Agency (project Labex STORE-EX, ANR-10-LABX-76-01).

A CC-BY public copyright license has been applied by the authors to the present document and will be applied to all subsequent versions up to the Author Accepted manuscript arising from this submission, in accordance with the grant's open access conditions.

5. REFERENCES

[1] T. Nagaura, K. Tozawa, Lithium ion rechargeable battery, Progress in Batteries and Solar Cells. 9 (1990) 209–217.

[2] J.T. Frith, M.J. Lacey, U. Ulissi, A non-academic perspective on the future of lithium-based batteries, Nat Commun. 14 (2023). https://doi.org/10.1038/s41467-023-35933-2.

[3] M.N. Obrovac, L. Christensen, Structural changes in silicon anodes during lithium insertion/extraction, Electrochemical and Solid-State Letters. 7 (2004). https://doi.org/10.1149/1.1652421.

[4] J. Asenbauer, T. Eisenmann, M. Kuenzel, A. Kazzazi, Z. Chen, D. Bresser, The success story of graphite as a lithium-ion anode material-fundamentals, remaining challenges, and recent developments including silicon (oxide) composites, Sustain Energy Fuels. 4 (2020) 5387–5416. https://doi.org/10.1039/d0se00175a.

[5] F. Ozanam, M. Rosso, Silicon as anode material for Li-ion batteries, Mater Sci Eng B Solid State Mater Adv Technol. 213 (2016) 2–11. https://doi.org/10.1016/j.mseb.2016.04.016.

[6] C.M. Hwang, C.H. Lim, J.W. Park, Evaluation of Si/Ge multi-layered negative film electrodes using magnetron sputtering for rechargeable lithium ion batteries, Thin Solid Films. 519 (2011) 2332–2338. https://doi.org/10.1016/j.tsf.2010.10.049.

[7] L.C. Loaiza, E. Salager, N. Louvain, A. Boulaoued, A. Iadecola, P. Johansson, L. Stievano, V. Seznec, L. Monconduit, Understanding the lithiation/delithiation mechanism of Si1-: XGex alloys, J Mater Chem A Mater. 5 (2017) 12462–12473. https://doi.org/10.1039/c7ta02100c.

[8] X.H. Liu, Y. Liu, A. Kushima, S. Zhang, T. Zhu, J. Li, J.Y. Huang, In situ TEM experiments of electrochemical lithiation and delithiation of individual nanostructures, Adv Energy Mater. 2 (2012) 722–741. https://doi.org/10.1002/aenm.201200024.

[9] L. Solymar, D. Walsh, Semiconductors, in: Electrical Properties of Materials, OUP Oxford, 2009: p. 464.

[10] E.M. Pell, Diffusion rate of Li in Si at low Temperatures, Physical Review. 119 (1960) 1222.

[11] F. C.S., Severiens J.C., Mobility of Impurity Ions in Germanium and Silicon, Quantum Statistics. 193 (1954).

[12] A. Desrues, J.P. Alper, F. Boismain, D. Zapata Dominguez, C. Berhaut, P.E. Coulon, A. Soloy, F. Grisch, S. Tardif, S. Pouget, S. Lyonnard, C. Haon, N. Herlin-Boime, Best Performing SiGe/Si Core-Shell Nanoparticles Synthesized in One Step for High Capacity Anodes, Batter Supercaps. 2 (2019) 970–978. https://doi.org/10.1002/batt.201900094.

[13] D. Duveau, B. Fraisse, F. Cunin, L. Monconduit, Synergistic effects of Ge and Si on the performances and mechanism of the GexSi1-x electrodes for Li ion batteries, Chemistry of Materials. 27 (2015) 3226–3233. https://doi.org/10.1021/cm504413g.

[14] X. Chen, L. Monconduit, V. Seznec, 2D Si-Ge layered materials as anodes for alkali-cation (Na+, K+) batteries, Electrochim Acta. 462 (2023) 142756. https://doi.org/10.1016/j.electacta.2023.142756.

[15] H. Chen, Y. Zheng, Q. Wu, W. Zhou, Q. Wei, M. Wei, Dual-carbon materials coated Ge/Si composite for high performance lithium-ion batteries, Electrochim Acta. 417 (2022) 140337. https://doi.org/10.1016/j.electacta.2022.140337.

[16] Z. yuan Feng, W. jie Peng, Z. xing Wang, H. jun Guo, X. hai Li, G. chun Yan, J. xi Wang, Review of silicon-based alloys for lithium-ion battery anodes, International Journal of Minerals, Metallurgy and Materials. 28 (2021) 1549–1564. https://doi.org/10.1007/s12613-021-2335-x.

[17] P. Yogi, M. Tanwar, S.K. Saxena, S. Mishra, D.K. Pathak, A. Chaudhary, P.R. Sagdeo, R. Kumar, Quantifying the Short-Range Order in Amorphous Silicon by Raman Scattering, Anal Chem. 90 (2018) 8123–8129. https://doi.org/10.1021/acs.analchem.8b01352.

[18] D. Tuschel, Why are the Raman spectra of crystalline and amorphous solids different?, Spectroscopy (Santa Monica). 32 (2017) 26–33.

[19] M.B. Heaney, Electrical Conductivity and Resistivity, in: Measurement, Instrumentation, and Sensors Handbook, CRC Press, Boca Raton, 2014: p. 1921. https://doi.org/10.1201/b15664.

[20] H. Wiggers, S. Hartner-Plumel, Nanotech Conference & Expo 2010 : technical proceedings of the 2010 NSTI Nanotechnology Conference and Expo : June 21-24, 2010, Anaheim, California, U.S.A., in: Electrical Properties of Functionalized Silicon Nanoparticles, Nano Science and Technology Institute, 2010: pp. 376–378.

[21] J.M. Montes, F.G. Cuevas, J. Cintas, P. Urban, Electrical conductivity of metal powders under pressure, Appl Phys A Mater Sci Process. 105 (2011) 935–947. https://doi.org/10.1007/s00339-011-6515-9.

[22] K. Ogata, E. Salager, C.J. Kerr, A.E. Fraser, C. Ducati, A.J. Morris, S. Hofmann, C.P. Grey, Revealing lithium-silicide phase transformations in nano-structured silicon-based lithium ion batteries via in situ NMR spectroscopy, Nat Commun. 5 (2014). https://doi.org/10.1038/ncomms4217.

[23] B. Key, M. Morcrette, J.M. Tarascon, C.P. Grey, Pair distribution function analysis and solid state NMR studies of silicon electrodes for lithium ion batteries: Understanding the (de)lithiation mechanisms, J Am Chem Soc. 133 (2011) 503–512. https://doi.org/10.1021/ja108085d.

[24] M.T. McDowell, S.W. Lee, J.T. Harris, B.A. Korgel, C. Wang, W.D. Nix, Y. Cui, In situ TEM of two-phase lithiation of amorphous silicon nanospheres, Nano Lett. 13 (2013) 758–764. https://doi.org/10.1021/nl3044508.

[25] N. Ding, J. Xu, Y.X. Yao, G. Wegner, X. Fang, C.H. Chen, I. Lieberwirth, Determination of the diffusion coefficient of lithium ions in nano-Si, Solid State Ion. 180 (2009) 222–225. https://doi.org/10.1016/j.ssi.2008.12.015.

[26] C. Keller, A. Desrues, S. Karuppiah, E. Martin, J.P. Alper, F. Boismain, C. Villevieille, N. Herlin-Boime, C. Haon, P. Chenevier, Effect of size and shape on electrochemical performance of nano-silicon-based lithium battery, Nanomaterials. 11 (2021) 1–15. https://doi.org/10.3390/nano11020307.

[27] X.H. Liu, L. Zhong, S. Huang, S.X. Mao, T. Zhu, J.Y. Huang, Size-Dependent Fracture of Silicon, ACS Nano. 6 (2012) 1522–1531.

[28] K. Pan, F. Zou, M. Canova, Y. Zhu, J.H. Kim, Systematic electrochemical characterizations of Si and SiO anodes for high-capacity Li-Ion batteries, J Power Sources. 413 (2019) 20–28. https://doi.org/10.1016/j.jpowsour.2018.12.010.

[29] M.N. Obrovac, L. Christensen, D.B. Le, J.R. Dahn, Alloy Design for Lithium-Ion Battery Anodes, J Electrochem Soc. 154 (2007) A849. https://doi.org/10.1149/1.2752985.

[30] B. Laforge, L. Levan-jodin, R. Salot, A. Billard, Study of Germanium as Electrode in Thin-Film Battery, (2008). https://doi.org/10.1149/1.2820666.

[31] A.M. Skundin, T.L. Kulova, A.B. Yaroslavtsev, Study of the Process of Reversible Insertion of Lithium into Nanostructured Materials Based on Germanium, Russian Journal of Electrochemistry. 54 (2018) 1111–1116. https://doi.org/10.1134/S1023193518020076.

[32] D. Zapata Dominguez, C.L. Berhaut, A. Buzlukov, M. Bardet, P. Kumar, P.H. Jouneau, A. Desrues, A. Soloy, C. Haon, N. Herlin-Boime, S. Tardif, S. Lyonnard, S. Pouget, (De)Lithiation and Strain Mechanism in Crystalline Ge Nanoparticles, ACS Nano. 16 (2022) 9819–9829. https://doi.org/10.1021/acsnano.2c03839.

[33] J. Li, N.J. Dudney, X. Xiao, Y.T. Cheng, C. Liang, M.W. Verbrugge, Asymmetric rate behavior of Si anodes for lithium-ion batteries: Ultrafast de-lithiation versus sluggish lithiation at high current densities, Adv Energy Mater. 5 (2015) 1–6. https://doi.org/10.1002/aenm.201401627.

[34] Y. Kubota, M.C.S. Escao, H. Nakanishi, H. Kasai, Crystal and electronic structure of Li15Si4, J Appl Phys. 102 (2007). https://doi.org/10.1063/1.2775999.

[35] P. Bärmann, B. Krueger, S. Casino, M. Winter, T. Placke, G. Wittstock, Impact of the Crystalline Li15Si4Phase on the Self-Discharge Mechanism of Silicon Negative Electrodes in Organic Electrolytes, ACS Appl Mater Interfaces. 12 (2020) 55903–55912. https://doi.org/10.1021/acsami.0c16742.

[36] I.M. Gavrilin, V.A. Smolyaninov, A.A. Dronov, S.A. Gavrilov, A.Y. Trifonov, Study of the Process of Reversible Insertion of Lithium into Nanostructured Materials Based on Germanium, 54 (2018) 1111–1116. https://doi.org/10.1134/S1023193518120054.